Foam–like Co$_9$S$_8$/Ni$_3$S$_2$ heterostructure nanowire arrays for efficient bifunctional overall water–splitting

Feng Du[a,d,1], Li Shi[c,1], Yintong Zhang[a,d,1], Tao Li[b,*], Jinlan Wang[c,**], Guihua Wen[e], Ahmed Alsaedi[f], Tasawar Hayat[f,g], Yong Zhou[a,d,h,***], Zhigang Zou[a,d,h]

[a] School of Physics, National Laboratory of Solid State Microstructures, Nanjing University, Nanjing, Jiangsu 210093, PR China
[b] Engineering Technology Research Center of Henan Province for Solar Catalysis, School of Chemistry and Pharmaceutical Engineering, Nanyang Normal University, Nanyang, Henan 473061, PR China
[c] School of Physics, Southeast University, Nanjing, Jiangsu 211189, PR China
[d] Jiangsu Key Laboratory for Nano Technology, Nanjing University, Nanjing, Jiangsu 210093, PR China
[e] Kunshan Sunlaite New Energy Co., LTd, Kunshan Innovation Institute of Nanjing University, Kunshan, Jiangsu 215347, PR China
[f] Faculty of Science, King Abdulaziz University, Jeddah 21589, Saudi Arabia
[g] Department of Mathematics, Quaid-I-Azam University, Islamabad 45320, Pakistan
[h] Kunshan Innovation Institute of Nanjing University, Kunshan, Jiangsu 215347, PR China

ARTICLE INFO

ABSTRACT

Foam–like nanowire arrays composed of the Co$_9$S$_8$/Ni$_3$S$_2$ heterostructure possess huge electrochemical surface areas and rich lattice defects. The value of double–layer capacitance for Co$_9$S$_8$/Ni$_3$S$_2$ is detected to be 81.4 m F·cm^{-2}, which is four times more than the precursor (Ni$_x$Co$_{1-x}$(CO$_3$)$_{0.5}$OH). This enhancement greatly produces a large number of catalytic reaction sites for contacting with electrolyte ions. The method of *in–situ* vulcanization growth urges the uniform distribution of Co$_9$S$_8$ and Ni$_3$S$_2$, forming a large number of lattice defects in the heterointerfaces. These lattice defects modulate the local electronic arrangement to become the most active reaction sites. Density functional theory calculations demonstrate that the defective heterointerfaces are beneficial to the chemisorption of H$^+$ and OH–. Electrochemical tests illustrate that Co$_9$S$_8$/Ni$_3$S$_2$ electrodes exhibit efficient activities for oxygen and hydrogen evolution reactions and have remarkable stabilities in alkaline solution for commercial application.

1. Introduction

The problems of traditional fossil fuel shortage and environmental pollution are increasingly serious. Hence it is extremely urgent to develop appropriate alternative power sources [1–3]. Hydrogen, a kind of renewable and clean energy, has been recognized as one of the most promising choices [4,5]. Among various methods of hydrogen production, electrochemical water splitting is a widely concerned way, because of the simple process and little pollution [6,7]. Noble metal (Pt) and noble metal oxide (RuO$_2$, IrO$_2$) have shown the most effectively catalytic activity for the two half reactions of overall water splitting, hydrogen evolution reaction (HER) and oxygen evolution reaction (OER) respectively [8–11]. However, considering the scarcity, they cannot be utilized in a large scale due to the scarcity [12]. Thus, many

researchers have focused on seeking the alternative materials [13].

Recently, transition metal hydroxides (M–OH) have gained a huge number of attentions due to their easily tunable chemical component and complex electronic structure. On the basis of M–OH, many optimized schemes with the introduction of defects have been reported. For example, nitrogen doping and defects were introduced into exfoliated ultrathin CoFe layered double hydroxides nanosheets, which could increase the number of reactive sites to enhance the OER activity [14]. Iridium (Ir) incorporated cobalt-based hydroxide nanosheets displayed highly efficient OER catalytic performance through the formation of rich Co–Ir species [15]. Most researches introduced the defects by stepwise heteroatom doping. These processes usually require complex synthesis steps and harsh experimental conditions. Furthermore, the stepwise introductions only change the surface electronic structure in

general. Unfortunately, transition metal hydroxides have a restricted performance for overall water splitting because of the inherent poor HER activity. Recently, sulfides have been proved in a large number of researches for highly H_2–evolution activities, such as nickel sulfides and cobalt sulfides [16–20]. Under coordinated Ni/Co sites on the surface are the efficient HER active part, which possess high chemisorption capability for hydrogen [21–24]. Therefore, *in–situ* vulcanizing NiCo hydroxide to form the defective heterointerfaces of Ni–S and Co–S can possess the synergistically promoted kinetics on varied active sites and electron–reconfigured interfaces. Meanwhile, it is necessary to design rational engineering, in which the defective heterointerfaces should be fully exposed and the system can be beneficial to the transmission of ion/electron [25–28]. In this respect, one–dimensional (1D) system can easily facilitate charge transfer in a radial direction and expose abundant active sites along the interconnecting networks [29–32]. In addition, the activity of water splitting is closely related to the amount of active sites. Loose porous structure will make more positions for contacting with electrolyte ions. Therefore, construction of 1D foam–like rich lattice defects Ni–Co–S heterostructure shows great potential for development of overall water splitting.

In this work, defect–enriching foam–like Co_9S_8/Ni_3S_2 nanowire arrays on 3D Ni substrate were successfully prepared and then acted as efficient bifunctional electrocatalysts for both OER and HER in 1.0 M KOH. *In–situ* vulcanization treatment greatly increased the electrochemical surface areas of the heterostructure, producing faster charge conduction paths and more reaction sites. Meanwhile, due to the co-existence of the two phases (Co_9S_8 and Ni_3S_2), a large number of lattice defects arose in the heterointerfaces, which were more conducive to the chemisorption of hydrogen and oxygen-containing intermediates, thus facilitating the overall electrochemical water-splitting activity. Density functional theory (DFT) calculations showed that the defective heterointerfaces possessed lower free energies of hydrogen (ΔG_H) and hydroxide (ΔG_{OH}), confirming foam–like Co_9S_8/Ni_3S_2 was indeed an efficient water–splitting electrocatalyst. Specifically, Co_9S_8/Ni_3S_2 electrodes exhibited the low η_{10} (at an O_2–evolution current density of 10 mA cm^{-2}) of 227 mV and η_{-10} (at a H_2–evolution current density of -10 mA cm^{-2}) of -128 mV. This bifunctional electrodes also enabled a high–efficiency two–electrode overall water–splitting at 10 mA cm^{-2} with a cell driven voltage of only 1.64 V. Additionally, constant current tests revealed it with excellent electrochemical durability for potential application value.

2. Experimental

2.1. Preparation of $Ni_xCo_{1-x}(CO_3)_{0.5}OH$ nanowire arrays

The $Ni_xCo_{1-x}(CO_3)_{0.5}OH$ nanowire arrays on Ni substrate was synthesized by hydrothermal reaction. Typically, a piece of Ni foam (1 cm × 6 cm) was cleaned by sonication sequentially in ethanol, acetone, 3 M HCl and deionized water for several times to make sure that nickel oxide on the surface was removed. $CoCl_2\cdot6H_2O$ (6 mmol) and urea (12 mmol) were dissolved in 35 mL deionized water with stirring until the solution was clean. Then the solution was transferred into a 50 mL Teflon–lined stainless–steel autoclave and a piece of surface–cleaned Ni foam was immersed after heating in an electric oven at 120 °C for 6 h, the Ni foam was taken out and washed by deionized water and ethanol to remove surface impurities.

2.2. Preparation of foam–like Co_9S_8/Ni_3S_2 nanowire arrays

The $Ni_xCo_{1-x}(CO_3)_{0.5}OH$ nanowire arrays on Ni substrate was put into 35 mL deionized water containing 7 mmol $Na_2S\cdot9H_2O$. Similarly, the solution was transferred into a 50 mL Teflon–lined stainless–steel autoclave, and maintained at 160 °C for 6 h. Finally, the Ni foam was cleaned by deionized water and ethanol and dried overnight.

By adding different amounts of Co source in the first hydrothermal reaction, five samples were synthesized for comparison to investigate the relationship between electrocatalytic performance and ratio of Co_9S_8 and Ni_3S_2. Specifically, in the first hydrothermal reaction process, the additive amounts of $CoCl_2\cdot6H_2O$ were 0.5, 1, 3, 6 and 9 mmol, respectively. With other synthetic conditions remained unchanged, the five products were labeled as Co-0.5, Co-1, Co-3, Co-6 and Co-9, respectively. Co-6 (or Co_9S_8/Ni_3S_2) exhibited the best activities for both OER and HER. The detailed discussion of the effect of Co source on the micro-structure and electrocatalytic performance can be found in the Supporting Information.

2.3. Characterization

Powder X–ray diffraction (XRD, Rigaku Ultima III, Cu Kα radiation) was used to identify the phase formation of as–synthesized samples. The morphologies were observed by a scanning electron microscope (SEM, Hitachi, S–3400NII), and more detailed morphology information and the elemental composition of the nanowires were examined by a transmission electron microscope (TEM, JEM–200CX). The X–ray photoelectron spectroscopy (XPS) measurements were performed on a PHI 5000 Versa Probe instrument with an Al Kα X–ray radiation. The specific surface area was investigated by nitrogen adsorption–desorption using the Brunauer–Emmett–Teller (BET) method (Micromeritics ASAP 2020).

2.4. Electrochemical measurements

All electrochemical tests were performed by an electrochemical workstation (CHI660E, Shanghai Chenhua). The synthesized samples were used as working electrode, the carbon rod was utilized as the counter electrode and an Ag/AgCl (3 M KCl solution) was served as the reference electrode. All measurements were performed in 1.0 M KOH aqueous electrolyte in room temperature. All linear–sweep voltammo-grams (LSV) were tested at a scan of 2 mV·s^{-1}, and the potential was converted by the use of equation $E_{RHE} = E_{Ag/AgCl} + 0.205 + 0.0591 \times$ pH. The electrochemical impedance spectroscopies (EIS) were carried out at a certain potential with the sweeping frequency range from 100 KHz to 0.1 Hz. The electrochemical surface area (ECSA) measurement was estimated through cyclic voltammograms (CV) by changing different scan rates. The stability was tested by controlling potential electrolysis. Overall water splitting test was carried out with a two–electrode system, with the Co_9S_8/Ni_3S_2 nanowires as anode and cathode at the same time.

2.5. DFT computational methods

All geometry optimizations and electronic structure calculations were performed using density functional theory (DFT) implemented in VASP [33,34], which uses the projected augmented wave (PAW) method [35]. The exchange–correlation interaction was described by generalized gradient approximation (GGA) with the Perdew − Burke − Ernzerhof (PBE) functional [36,37]. The spin–polarization effect is included in all calculations. The electron wave functions were expanded using plane waves with an energy cutoff of 450 eV and the convergence threshold was 10^{-4} eV for energy and 0.02 eV Å^{-1} for force, respectively. Slab model was used for all calculations with a vacuum thickness of 16 Å to avoid the interaction between two periodic units.

The catalytic activity of materials can be determined by the free energy of different adsorbed species. The free energy of adsorbed species in this work is defined as: $\Delta G_M = \Delta E_M + \Delta E_{zpe} - T\Delta S$, where ΔE_M (M = *H and *OH) is the adsorption energy of adsorbed species. The absorption energies were calculated according to the formula: $\Delta E_H = E_{(plane + H)} - E_{(plane)} -1/2 E_{H2}$, $\Delta E_{OH} = E_{(plane + OH)} - E_{(plane)} - (E_{H2O}-1/2 E_{H2})$. E_{H2O} and E_{H2} are the calculated DFT energies of H_2O and H_2 molecules in the gas phase. The ΔE_{zpe} is the difference in zero point
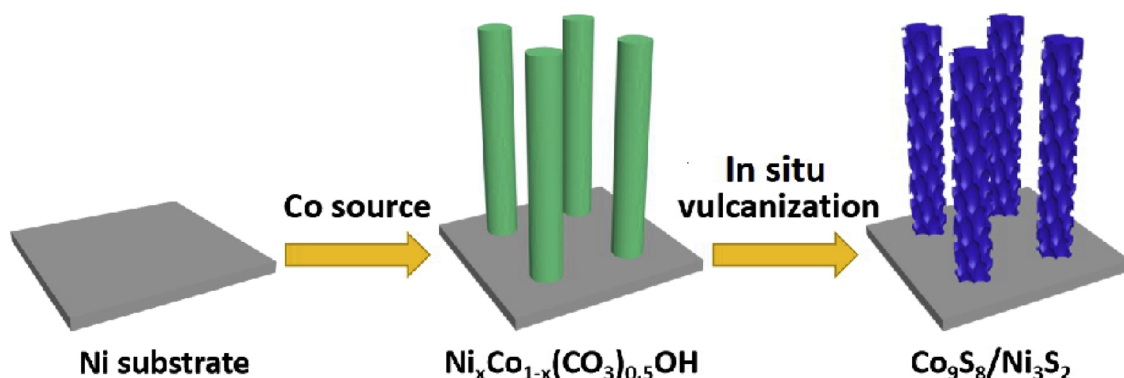
Fig. 1. Schematic representation of the synthesis of foam–like Co_9S_8/Ni_3S_2 nanowire arrays.

energies due to the reaction and ΔS is the change in entropy, T is the temperature (room temperature adopted in this work).

3. Results and discussion

Fig. 1 shows the synthesis process of electrocatalysts. In the first step, cobaltous chloride provided Co source, and Ni source came from the Ni substrate. After the hydrothermal reaction for 6 h, the precursor presented nanowires structure with smooth surfaces. Then, the second hydrothermal process made the nanowires expand and removal of oxygen group to form foam–like structure. Meanwhile, *in–situ* vulcanization treatment facilitated the uniform distribution of the two phases (Co_9S_8 and Ni_3S_2) to form a large number of heterointerfaces. Fig. 2a presents the X–ray diffraction (XRD) patterns of the as–prepared precursor and electrocatalyst. For the patterns of all samples, the strong peaks located at $2\theta = 44.8°$ and $52.1°$ could be assigned to the (111) and (200) planes of Ni foam substrate, respectively (JCPDF: 04-0850). The diffraction peaks of precursor ($Ni_xCo_{1-x}(CO_3)_{0.5}OH$) could be well matched with $Co(CO_3)_{0.5}OH$ (JCPDS No. 48–0083), but slightly shifted to the low–angle direction (Fig. S1c, Supporting information). The shift was due to the partial substitution of Co ions by Ni ions, leading to the slight change of the lattice parameters [38,39]. For the electrocatalyst (Co_9S_8/Ni_3S_2), the characteristic peaks at 2θ values of $29.7°$, $47.6°$, $51.9°$ and $61.3°$ could be well identified as the Co_9S_8 phase (JCPDS No. 19–0364), and the peaks at $21.6°$, $30.9°$, $37.8°$, $49.6°$ and $55.1°$ could be assigned to the heazlewoodite Ni_3S_2 phase (JCPDS No. 44–1418) (Fig. S1d). It was obvious that the signals from $NiCo(CO_3)_{0.5}OH$ disappeared in the Co_9S_8/Ni_3S_2 samples, indicating that the precursor had evolved into sulfides completely after *in–situ* vulcanization treatment. The results confirmed the coexistence of the two phases (Co_9S_8 and Ni_3S_2) clearly. The SEM images of $Ni_xCo_{1-x}(CO_3)_{0.5}OH$ presented a large amount of nanowires, which looked like cluttered grass and have smooth surfaces (Fig. 2b, c and S2). Co_9S_8/Ni_3S_2 had a similar feature by and large (Fig. 2d, e and S2). The difference between them was just the surface of Co_9S_8/Ni_3S_2 exhibiting roughness and unsmoothness, which was beneficial to expose more active sites. These nanowires possessed a mean diameter of about 200 nm and a long length along the directional growth. They contacted with the conductive substrate directly (Fig. S3) to benefit direct electron transport between the catalyst and current collector, decreasing the contact resistance and ensuring effectively participate in the electrochemical reactions [40]. Fig. 2f presents the TEM images of Co_9S_8/Ni_3S_2 nanowires detached ultrasonically from the Ni substrate. The heterojunction catalyst showed roughness and hollow characteristics. The reason for forming the foam–like structure was attributed to the hydrothermal vulcanization process, which can expand the nanowires and remove oxygen groups. This especial 1D foam characteristic would provide a large active surface area, which could easily contact with electrolyte ions to promote the electrochemical reactions. The selected area electron diffraction (SAED) of Co_9S_8/Ni_3S_2 clearly showed two different diffraction patterns

(Fig. 2g). The polycrystalline rings (white rings) were well matched with (110), (202) and (122) planes of Ni_3S_2, and diffraction spots (yellow circles) were attributed to (220), (222), (420) and (440) plane of Co_9S_8. The high–resolution TEM (HRTEM) images (Fig. S4) revealed that the two phases of Co_9S_8 and Ni_3S_2 distributed uniformly and the size of each phase is about 20 nm. These lattice fringes were in good agreement with the XRD results. Specially, amorphous regions could be easily found in the interfaces between Co_9S_8 and Ni_3S_2 (red line area, Fig. 2h). There were many lattice defects in the amorphous regions, and these defects caused the change of local electronic structure, which were propitious to the actual catalytic performance. By analyzing the micro region phase characteristics, Co_9S_8/Ni_3S_2 was considered as the mixed polycrystalline form. Spectrums of energy dispersive spectroscopy (EDS) mappings (Fig. 2i) and line scanning (Fig. S5) revealed a coincided distribution of Co, Ni and S elements in Co_9S_8/Ni_3S_2, and further confirmed the coexistence of the mixed two phases, illustrating the notion of foam–like nanowires heterostructure.

The electrocatalytic OER activity of Co_9S_8/Ni_3S_2 was assessed in 1.0 MKOH using a standard three electrode system. Meanwhile, bare NF (Ni substrate foam), Ni_3S_2 (obtained by direct vulcanizing NF) and $Ni_xCo_{1-x}(CO_3)_{0.5}OH$ electrode were prepared and tested under identical conditions. Linear sweep voltammetry (LSV) polarization curves revealed significant differences in the OER activities of the various electrocatalysts (Fig. 3a). Here, Co_9S_8/Ni_3S_2 exhibited a low overpotential of 227 mV at the current density of $10\ \text{mA·cm}^{-2}$ (η_{10}) (Fig. S9), which compared favorably with many recent reported non–precious electrocatalysts listed in Table S1. The corresponding Tafel plots were estimated in Fig. 3b. An excellent value of $46.5\ \text{mV·dec}^{-1}$ for Co_9S_8/Ni_3S_2 was superior to NF ($128.7\ \text{mV·dec}^{-1}$), Ni_3S_2 ($99.3\ \text{mV·dec}^{-1}$), $Ni_xCo_{1-x}(CO_3)_{0.5}OH$ ($69.7\ \text{mV·dec}^{-1}$). All these results demonstrated that the as–prepared rich lattice defects foam–like Co_9S_8/Ni_3S_2 exhibited excellent OER electrocatalysis performance compared with the reported Ni−Co−S−based electrocatalysts (Fig. S10), also ranking one of the superior non–noble metal–based electrocatalyst in KOH. As for HER, Co_9S_8/Ni_3S_2 also presented a high activity, with the low overpotential (η_{-10}) of -128 mV (Fig. 3c). The performance was better than many reported electrocatalysts listed in Table S2. Ni_3S_2 and $Ni_xCo_{1-x}(CO_3)_{0.5}OH$ gave the poor overpotentials of -222 and -230 mV, respectively. Fig. 3d provides the corresponding Tafel plots of various samples. Co_9S_8/Ni_3S_2 exhibited the lowest value ($97.6\ \text{mV dec}^{-1}$) than other electrocatalysts, illustrating more favorable HER kinetics. In contrast to many reported N−Co−S−based electrocatalysts (Fig. S11), Co_9S_8/Ni_3S_2 also exhibited great advantages.

The long–term electrochemical stability of Co_9S_8/Ni_3S_2 was tested at the constant current density of $10\ \text{mA·cm}^{-2}$ for OER and $-10\ \text{mA·cm}^{-2}$ for HER, respectively (Fig. 3e). The results showed negligible decay in the value of the static potential, illustrating excellent electrocatalytic durability. Meanwhile, a two–electrode electrolyzer system using the heterojunction catalyst as both anode and cathode ($Co_9S_8/Ni_3S_2//Co_9S_8/Ni_3S_2$) had been constructed to develop a real
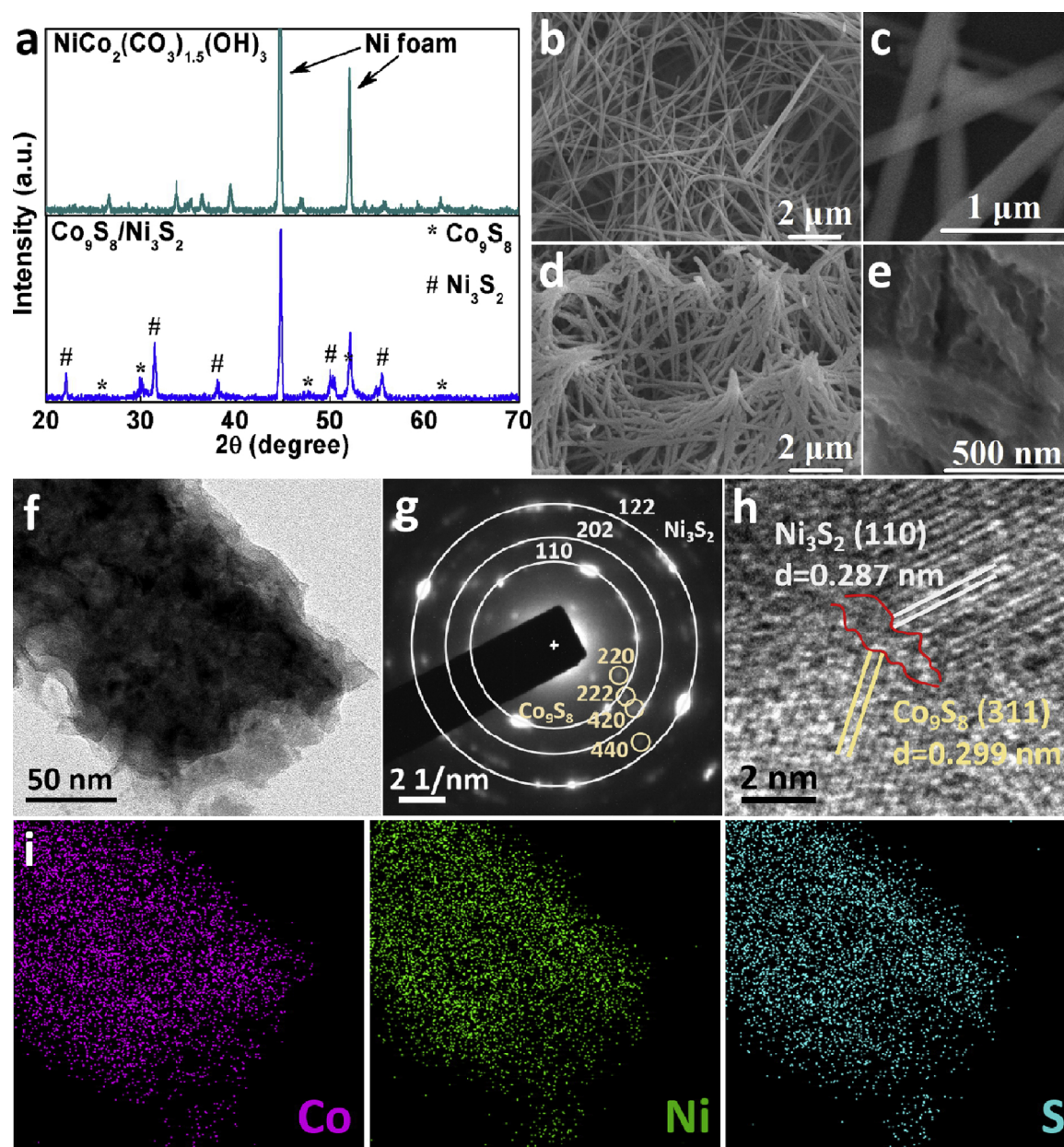
Fig. 2. (a) XRD patterns of $Ni_xCo_{1-x}(CO_3)_{0.5}OH$ and Co_9S_8/Ni_3S_2. SEM images of (b and c) $NixCo_{1-x}(CO_3)_{0.5}OH$, (d and e) Co_9S_8/Ni_3S_2. (f) TEM, (g) SAED pattern and (h) HRTEM image of Co_9S_8/Ni_3S_2. (i) EDS mappings of Co, Ni and S elements for Co_9S_8/Ni_3S_2.

overall water–splitting process in 1.0 M KOH. The polarization curves (Fig. 3f) indicated the Co_9S_8/Ni_3S_2 electrode exhibited superior overall water–splitting activity. Remarkably, a current density of 10 mA·cm^{-2} could be achieved with an overpotential as low as a cell voltage of 1.64 V, which was considerably lower than $Ni_xCo_{1-x}(CO_3)_{0.5}OH$ and also superior to many recent reported electrocatalysts listed in Table S3. The boosting electrocatalytic activity might be due to the coexistence of the two phases, which produced a larger amount of lattice defects and modulated the electronic arrangement of the heterointerfaces to accelerate the decomposition of water. Furthermore, foam–like structure produced fast electron conduction paths and large number of active sites for contacting with electrolyte ions to promote the electrochemical reactions. Last, the two–electrode cell durability also exhibited a great performance for 12 h of continuous electrolysis testing (Fig. S13).

To prove the electronic interactions of Co_9S_8 and Ni_3S_2, XPS spectra of Co_9S_8/Ni_3S_2 were measured with the $Ni_xCo_{1-x}(CO_3)_{0.5}OH$ as the reference. For the Co 2p spectrum (Fig. 4a), the peaks locating at 776.4

and 782.5 eV in the first doublet and the peaks at 792.6 and 798.1 eV in the second doublet corresponded to spin–orbit splitting values of Co $2p_{3/2}$ and Co $2p_{1/2}$, respectively, which could be assigned to Co^{3+} and Co^{2+}.[33] The weak satellite peaks indicated that the majority of Co atoms were in the Co^{3+} state [41–43]. In Ni 2p XPS spectrum (Fig. 4b), two main peaks at 873.7 and 856.8 eV were ascribed to Ni $2p_{1/2}$ and Ni $2p_{3/2}$, respectively, which were due to the coexistence of Ni^{2+} and Ni^{3+} species [44,45]. Compared with $Ni_xCo_{1-x}(CO_3)_{0.5}OH$, the binding energies of Co species and Ni species of Co_9S_8/Ni_3S_2 shifted positively, illustrating uniform distribution of two phases caused the modification of the electronic arrangement and then produced a strong electronic interaction in heterointerfaces [46–49]. In the high–resolution spectrum of S 2p spectrum of Co_9S_8/Ni_3S_2 (Fig. 4c), the peaks at 161.5 and 163.4 eV corresponded to S $2p_{3/2}$ and S $2p_{1/2}$ binding energies, respectively. The component peak at 165.1 eV was typical of a metal–sulfur (M−S) bond in the material [50].

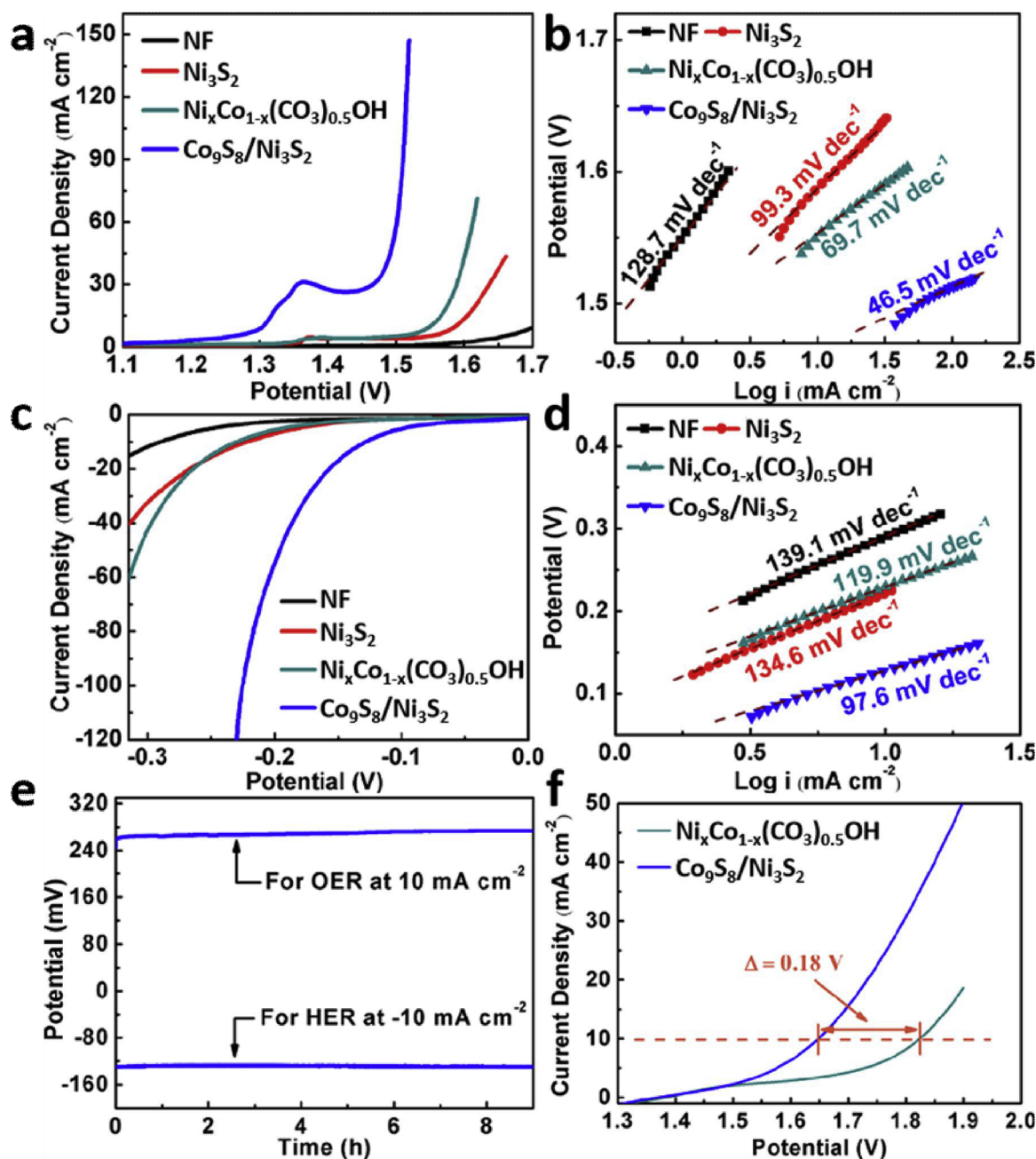To assess the effective active areas of foam–like Co_9S_8/Ni_3S_2, a

Fig. 3. (a) OER polarization curves, (b) corresponding OER Tafel plots, (c) HER polarization curves and (d) corresponding HER Tafel plots of NF, Ni_3S_2, $Ni_xCo_{1-x}(CO_3)_{0.5}OH$ and Co_9S_8/Ni_3S_2. (e) Chronopotentiometric durability of Co_9S_8/Ni_3S_2 for OER and HER. (f) Two electrode polarization curves with a scan rate 2 mV s^{-1} for $Co_9S_8/Ni_3S_2//Co_9S_8/Ni_3S_2$ and $Ni_xCo_{1-x}(CO_3)_{0.5}OH// Ni_xCo_{1-x}(CO_3)_{0.5}OH$.

series of cyclic voltammetry measurements were performed at scan rates varying from 30 mV·s^{-1} to 100 mV·s^{-1} in the region from 0.58 to 0.68 V versus the RHE (Figs. 4d and S15). The double–layer capacitances (C_{dl}) of various as–prepared electrocatalysts were obtained to characterize the electrochemical surface area (ECSA, Fig. 4e) [51,52]. As results, the values of, Ni_3S_2, $Ni_xCo_{1-x}(CO_3)_{0.5}OH$ and Co_9S_8/Ni_3S_2 were 2.8, 20.9 and 81.4 m F·cm^{-2}, respectively (Fig. 4f). Obviously, after hydrothermal vulcanization process, the C_{dl} achieved very remarkable promotion, suggesting Co_9S_8/Ni_3S_2 had the considerably highest electrochemical surface area, which was derived from the foam–like characteristic contributing to the significantly enhanced number of active sites [41,42]. Meanwhile, the Brunauer-Emmett-Teller (BET) specific surface area of Co_9S_8/Ni_3S_2 was calculated to be 3.4142 m^2 g^{-1} (Fig. S16), which was about 5.5 times bigger than $Ni_xCo_{1-x}(CO_3)_{0.5}OH$ (0.6344 m^2 g^{-1}). The result was consistent with the ECSA test.

Electrochemical impedance spectroscopy (EIS, Fig. S17) were also performed in a 1.0 M KOH solution at overpotentials of 0.405 V for OER and -1.225 V for HER. The variance in the charge transfer resistances (R_{ct}) derived from the semicircles in the low range of Nyquist plots [53]. The variety of charge transfer resistances of these electrocatalysts were also consistent with water–splitting kinetics, and Co_9S_8/Ni_3S_2 showed the smallest R_{ct} (0.03 Ω for OER and 1.89 Ω for HER, respectively), suggesting the fastest charger transfer process during water electrolysis of the foam–like electrocatalyst [54].

To better illustrate the catalytic performance of interfaces on the chemisorption of hydrogen and hydroxide intermediates, we further carried out DFT calculations to evaluate the free energies of hydrogen (ΔG_H) and hydroxide (ΔG_{OH}) on the (110) surface of Ni_3S_2 / Co–doped Ni_3S_2 and (311) surface of Co_9S_8 / Ni–doped Co_9S_8 (See Fig. 5a and Fig. S18). As we know, the Gibbs free energy ($|\Delta G_H|$) of the adsorbed H* is
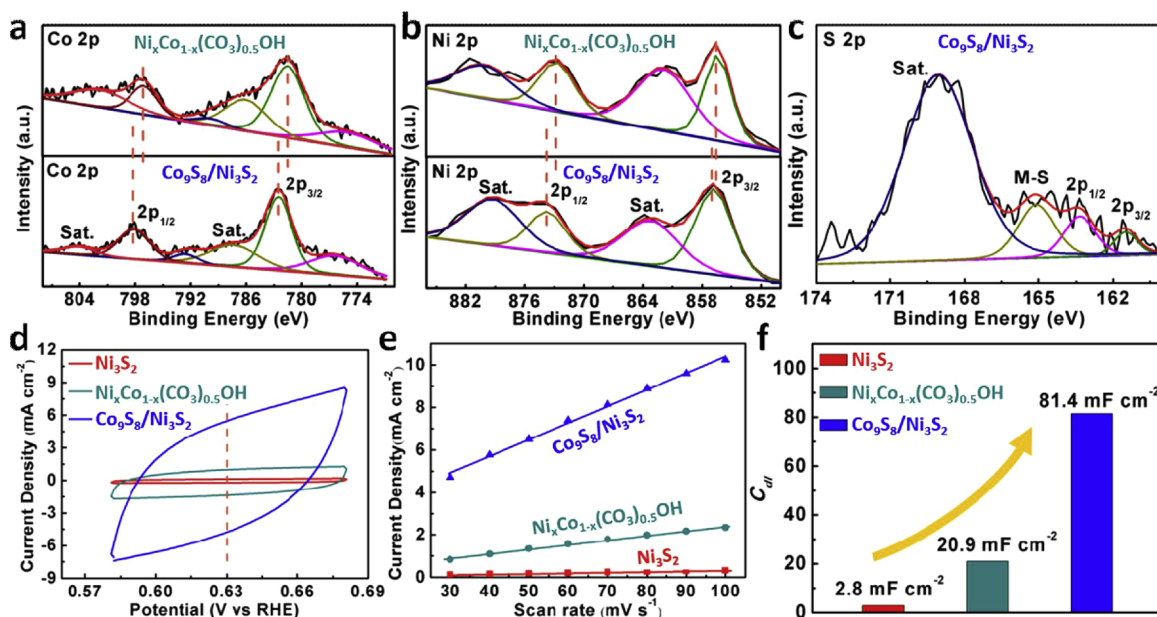
Fig. 4. XPS spectra of (a) Co 2p, (b) Ni 2p and (c) S 2p for $Ni_xCo_{1-x}(CO_3)_{0.5}OH$ and Co_9S_8/Ni_3S_2. (d) CV curves obtained at a scan rate of 100 mV·s^{-1} in the region of 0.58–0.68 V versus the RHE, (e) capacitive currents at 0.63 V versus RHE capacitive current at 0.15 V as a function of scan rate in 1.0 M KOH and (f) C_{dl} values of Ni_3S_2, $Ni_xCo_{1-x}(CO_3)_{0.5}OH$ and Co_9S_8/Ni_3S_2.

widely used to evaluate the HER activity, and the ideal value for HER is $|\Delta G_H| \approx 0$, which means that a smaller value of $|\Delta G_H|$ is expected to show a higher HER activity. As shown in Fig. 5a, for the Ni_3S_2 (110) surface, its surface is simple and there is only one kind of catalytic site. The calculated ΔG_H is as large as 0.42 eV (See Fig. 5b), suggesting the defect–free Ni_3S_2 (110) surface owns poor HER activity. This may be because S sites of Ni_3S_2 (110) surface are saturated and there is no more electron to bind H. However, for the case of Co_9S_8/Ni_3S_2 hetero-structure, the X–ray spectroscopy, TEM and EDS evidences show that Co atoms are doped into Ni_3S_2 matrix at the interface. Therefore, we constructed a metal (metal = Co) –doped model to simulate the heterostructure interface for the calculation. Bader charge analysis revealed that more electrons are injected into surface S sites (0.02e from Co to S sites), resulting in the ΔG_H (0.1 and 0.18 eV) much lower than that of defect–free Ni_3S_2 (110) and more closer to 0 eV (See Fig. 5b). This also indicates that it would have good performance for HER on the

interface of Co_9S_8/Ni_3S_2, consistent with our experimental results. In case of Co_9S_8 (311), the $|\Delta G_H|$ on the S sites is lower than that on Co sites, inferring that only S atoms of Co_9S_8 (311) are the possible active sites. The very negative ΔG_H on Co sites demonstrate that the strong binding strength of H would lead to the slow release of the gaseous H_2 product. For Ni–doped Co_9S_8 (311), four kinds of possible doped sites were considered in our model (See Fig. 5a). The ΔG_H of all possible catalytic sites were calculated and two kinds of S sites of Ni3 and Ni4–substitution own ultralow $|\Delta G_H|$ with the values of 0.02 and 0.07 eV, respectively. Therefore, we can conclude that the interface of Ni_3S_2/Co_9S_8 exhibits much better HER catalytic efficiency than the surface of Co_9S_8 (311). In addition, as an important factor in evaluating OER activity, the adsorption energy of OH^- on the catalyst was also calculated. As shown in Fig. 5b, in case of Ni_3S_2 (110), the interfacial (Co1 and Co2–doped sites) adsorption ability of OH^- is stronger than that of Ni_3S_2 (110), which demonstrates the performance of OER will be
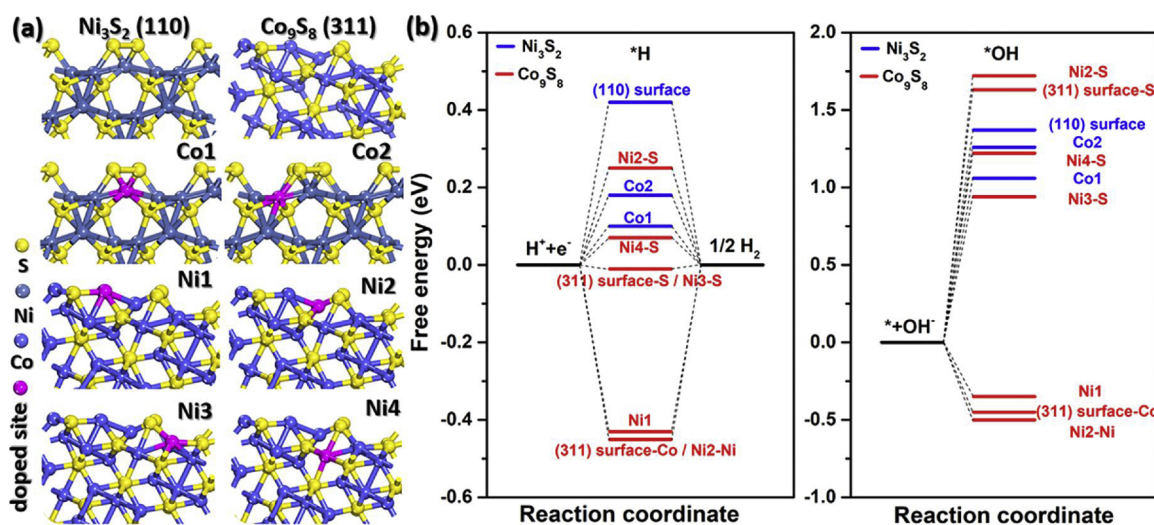

Fig. 5. (a) Schematic models of Ni_3S_2 (110), Co_9S_8 (311), Co-doped Ni_3S_2 (110) surface with two kinds of Co substitution sites and Ni-doped Co_9S_8 (311) surface with four kinds of Ni-substitution, respectively. (b) DFT-calculated free energy diagrams of hydrogen and hydroxide on Ni_3S_2 (110), Co_9S_8 (311), Co-doped Ni_3S_2 (110) and Ni-doped Co_9S_8 (311), respectively. Co1, Co2, Ni1, Ni2, Ni3 and Ni4 represent doped metal sites.

improved after Co is doped into Ni_3S_2 (110). As for the Co_9S_8 (311), the Co–sites of Co_9S_8 (311) show low OH^- adsorption free energies. Nevertheless, for the interface with forming Ni–doped Co_9S_8 (311), OH^- can easily adsorb onto metal (Ni1 and Ni2–doped sites) sites. In particular, the Ni2–doped sites show the strongest adsorption of OH^-, indicating the Ni2–doped sites (on the interface of Co_9S_8/Ni_3S_2) will be a better catalytic site for OER. The great agreement between theoretical calculation and experimental measurement of the catalytic reactions demonstrate that rich lattice defects foam–like Co_9S_8/Ni_3S_2 is, indeed, an efficient water–splitting electrocatalyst.

4. Conclusions

Defects–enriching foam–like Co_9S_8/Ni_3S_2 nanowire arrays had been successfully prepared through *in–situ* vulcanization method, and explored as efficient bifunctional electrocatalysts in strongly alkaline. The results showed that a large number of lattice defects in the heterointerfaces of Co_9S_8 and Ni_3S_2 led to strong electronic interaction, which promoted the function of the heterointerfaces on the chemisorption of hydrogen and oxygen-containing intermediates. Meanwhile, the unique foam–like structure possessed the synergistically promoted kinetics to produce fast electron conduction paths and many active response sites. Therefore, the as-prepared foam–like Co_9S_8/Ni_3S_2 electrode achieved an excellent performance for water splitting combined with an outstanding stability as compared to recently reported earth-abundant electrocatalysts. Therefore, this synthetic strategy and defective heterointerfaces engineering provided a favorable direction for potential application value in water splitting and would also be promising candidate in photochemical, photoelectrochemical and electrochemical N_2 and CO_2 reduction.

Acknowledgements

Appendix A. Supplementary data

Supplementary material related to this article can be found, in the online version, at doi:https://doi.org/10.1016/j.apcatb.2019.04.067.

References

[1] X. Zou, Y. Zhang, Chem. Soc. Rev. 44 (2015) 5148–5180.
[2] C.G. Morales-Guio, L.A. Stern, X. Hu, Chem. Soc. Rev. 43 (2014) 6555–6569.
[3] T. Wu, J. Fan, Q. Li, P. Shi, Q. Xu, Y. Min, Adv. Energy Mater. 8 (2018) 1701799.
[4] Z.H. Xue, H. Su, Q.Y. Yu, B. Zhang, H.H. Wang, X.H. Li, J.S. Chen, Adv. Energy Mater. 7 (2017) 1602355.
[5] S. Gong, Z. Jiang, P. Shi, J. Fan, Q. Xu, Y. Min, Appl. Catal. B: Environ. 238 (2018) 318–327.
[6] X. Gao, H. Zhang, Q. Li, X. Yu, Z. Hong, X. Zhang, C. Liang, Z. Lin, Angew. Chem. Int. Ed. Engl. 128 (2016) 6398–6402.
[7] W. Cui, Q. Liu, Z. Xing, A.M. Asiri, K.A. Alamry, X. Sun, Appl. Catal. B: Environ. 164 (2015) 144–150.
[8] H. Wang, H.W. Lee, Y. Deng, Z. Lu, P.C. Hsu, Y. Liu, D. Lin, Y. Cui, Nat. Commun. 6 (2015) 7261.
[9] R. Zhang, X. Wang, S. Yu, T. Wen, X. Zhu, F. Yang, X. Sun, X. Wang, W. Hu, Adv. Mater. 29 (2017) 1605502.
[10] H. Zhang, X. Li, A. Hähnel, V. Naumann, C. Lin, S. Azimi, S.L. Schweizer, A.W. Maijenburg, R.B. Wehrspohn, Adv. Funct. Mater. 28 (2018) 1706847.
[11] S. Gupta, N. Patel, R. Fernandes, R. Kadrekar, A. Dashora, A.K. Yadav, D. Bhattacharyya, S.N. Jha, A. Miotello, D.C. Kothari, Appl. Catal. B: Environ. 192 (2016) 126–133.
[12] T. Wu, Y. Ma, Z. Qu, J. Fan, Q. Li, P. Shi, Q. Xu, Y. Min, ACS Appl. Mater. Interfaces 11 (2019) 5136–5145.
[13] Y. Zheng, Y. Jiao, M. Jaroniec, S.Z. Qiao, Angew. Chem. Int. Ed. Engl. 54 (2015) 52.
[14] Y. Wang, C. Xie, Z. Zhang, D. Liu, R. Chen, S. Wang, Adv. Funct. Mater. 28 (2018) 1703363.
[15] Y. Zhang, C. Wu, H. Jiang, Y. Lin, H. Liu, Q. He, S. Chen, T. Duan, L. Song, Adv. Mater. 30 (2018) 1707522.
[16] X.Y. Yu, L. Yu, H.B. Wu, X.W. Lou, Angew. Chem. 127 (2015) 5421–5425.
[17] L.L. Feng, G. Yu, Y. Wu, G.D. Li, H. Li, Y. Sun, T. Asefa, W. Chen, X. Zou, J. Am. Chem. Soc. 137 (2015) 14023–14026.
[18] Y. Wu, X. Liu, D. Han, X. Song, L. Shi, Y. Song, S. Niu, Y. Xie, J. Cai, S. Wu, J. Kang, J. Zhou, Z. Chen, X. Zheng, X. Xiao, G. Wang, Nat. Commun. 9 (2018) 1425.
[19] Y. Liu, Q. Li, R. Si, G.D. Li, W. Li, D.P. Liu, D. Wang, L. Sun, Y. Zhang, X. Zou, Adv. Mater. 29 (2017) 1606200.
[20] Q. Xu, H. Jiang, H. Zhang, Y. Hu, C. Li, Appl. Catal. B: Environ. 242 (2019) 60–66.
[21] J. Zhang, T. Wang, D. Pohl, B. Rellinghaus, R. Dong, S. Liu, X. Zhuang, X. Feng, Angew. Chem. 128 (2016) 6814–6819.
[22] Q. Liu, J. Tian, W. Cui, P. Jiang, N. Cheng, A.M. Asiri, X. Sun, Angew. Chem. Int. Ed. Engl. 53 (2014) 6710–6714.
[23] S. Peng, L. Li, X. Han, W. Sun, M. Srinivasan, S.G. Mhaisalkar, F. Cheng, Q. Yan, J. Chen, S. Ramakrishna, Angew. Chem. Int. Ed. Engl. 126 (2014) 12802–12807.
[24] L.L. Feng, M. Fan, Y. Wu, Y. Liu, G.D. Li, H. Chen, W. Chen, D. Wang, X. Zou, J. Mater. Chem. A 4 (2016) 6860–6867.
[25] Z. Zhang, Q. Wang, C. Zhao, S. Min, X. Qian, ACS Appl. Mater. Interfaces 7 (2015) 4861–4868.
[26] S. Gong, Z. Jiang, P. Shi, J. Fan, Q. Xu, Y. Min, Appl. Catal. B: Environ. 238 (2018) 318–327.
[27] R. Li, S. Wang, J. Wang, Z. Huang, Phys. Chem. Chem. Phys. 17 (2015) 16434–16442.
[28] B. Liu, L. Jin, H. Zheng, H. Yao, Y. Wu, A. Lopes, J. He, ACS Appl. Mater. Interfaces 9 (2017) 1746–1758.
[29] Z. Peng, D. Jia, A.M. Al-Enizi, A.A. Elzatahry, G. Zheng, Adv. Energy Mater. 5 (2015) 1402031.
[30] H. Lin, Z. Shi, S. He, X. Yu, S. Wang, Q. Gao, Y. Tang, Chem. Sci. 7 (2016) 3399–3405.
[31] H. Lv, X. Chen, D. Xu, Y. Hu, H. Zheng, S.L. Suib, B. Liu, Appl. Catal. B: Environ. 238 (2018) 525–532.
[32] H. Lv, Y. Wang, A. Lopes, D. Xu, B. Liu, Appl. Catal. B: Environ. 249 (2019) 116–125.
[33] G. Kresse, J. Furthmüller, Phys. Rev. B Condens. Matter Mater. Phys. 54 (1996) 11169–11186.
[34] G. Kresse, D. Joubert, Phys. Rev. B Condens. Matter Mater. Phys. 59 (1999) 1758–1775.
[35] P.E. Blöchl, Phys. Rev. B Condens. Matter Mater. Phys. 50 (1994) 17953–17979.
[36] J.P. Perdew, Y. Wang, Phys. Rev. B Condens. Matter Mater. Phys. 45 (1992) 13244–13249.
[37] J.P. Perdew, J.A. Chevary, S.H. Vosko, K.A. Jackson, M.R. Pederson, D.J. Singh, C. Fiolhais, Phys. Rev. B Condens. Matter Mater. Phys. 46 (1992) 6671–6687.
[38] B. Yang, L. Yu, H. Yan, Y. Sun, Q. Liu, J. Liu, D. Song, S. Hu, Y. Yuan, L. Liu, J. Wang, J. Mater. Chem. A 3 (2015) 13308–13316.
[39] J. Yang, C. Yu, X. Fan, C. Zhao, J. Qiu, Adv. Funct. Mater. 25 (2015) 2109–2116.
[40] B. Zhu, S. Tang, S. Vongehr, H. Xie, J. Zhu, X. Meng, Chem. Commun. 52 (2016) 2624–2627.
[41] A. Sivanantham, P. Ganesan, S. Shanmugam, Adv. Funct. Mater. 26 (2016) 4661–4672.
[42] X. Dai, K. Du, Z. Li, M. Liu, Y. Ma, H. Sun, X. Zhang, Y. Yang, ACS Appl. Mater. Interfaces 7 (2015) 27242–27253.
[43] W. Kong, C. Lu, W. Zhang, J. Pu, Z. Wang, J. Mater. Chem. A 3 (2015) 12452–12460.
[44] X. Xiong, G. Waller, D. Ding, D. Chen, B. Rainwater, B. Zhao, Z. Wang, M. Liu, Nano Energy 16 (2015) 71–80.
[45] H. Liu, X. Ma, Y. Rao, Y. Liu, J. Liu, L. Wang, M. Wu, ACS Appl. Mater. Interfaces 10 (2018) 10890–10897.
[46] S. Yin, W. Tu, Y. Sheng, Y. Du, M. Kraft, A. Borgna, R. Xu, Adv. Mater. 30 (2018) 1705106.
[47] Q. Wang, L. Shang, R. Shi, X. Zhang, Y. Zhao, G. Waterhouse, L. Wu, C. Tung, T. Zhang, Adv. Energy Mater. 7 (2017) 1700467.
[48] H. Xu, B. Wang, C. Shan, P. Xi, W. Liu, Y. Tang, ACS Appl. Mater. Interfaces 10 (2018) 6336–6345.
[49] Q. Chen, C. Hou, C. Wang, X. Yang, R. Shi, Y. Chen, Chem. Commun. 54 (2018) 6400.
[50] W. Wei, L. Mi, S. Cui, B. Wang, W. Chen, ACS Sustain. Chem. Eng. 3 (2015) 2777–2785.
[51] X.L. Wang, L.Z. Dong, M. Qiao, Y.J. Tang, J. Liu, Y. Li, S.L. Li, J.X. Su, Y.Q. Lan, Angew. Chem. Int. Ed. 57 (2018) 9660–9664.
[52] F. Yu, H. Zhou, Y. Huang, J. Sun, F. Qin, J. Bao, W.A. GoddardIII, S. Chen, Z. Ren, Nat. Commun. 9 (2018) 2551.
[53] K. Liao, S. Chen, H. Wei, J. Fan, Q. Xu, Y. Min, J. Mater. Chem. A 6 (2018) 23062–23070.
[54] C. Guan, X. Liu, W. Ren, X. Li, C. Cheng, J. Wang, Adv. Energy Mater. 7 (2017) 1602391.